Development of a temperature-variable magnetic resonance imaging system using a 1.0 Tesla yokeless permanent magnet

Y. Terada*, D. Tamada, and K. Kose

Institute of Applied Physics, University of Tsukuba, Tsukuba, Ibaraki 305-8573, Japan,

Abstract

A temperature variable magnetic resonance imaging (MRI) system has been developed using a 1.0 T permanent magnet. A permanent magnet, gradient coils, radiofrequency coil, and shim coil were installed in a temperature variable thermostatic bath. First, the variation in the magnetic field inhomogeneity with temperature was measured. The inhomogeneity has a specific spatial symmetry, which scales linearly with temperature, and a single-channel shim coil was designed to compensate for the inhomogeneity. The inhomogeneity was drastically reduced by shimming over a wide range of temperature from –5 °C to 45 °C. MR images of an okra pod acquired at different temperatures demonstrated the high potential of the system for visualizing thermally sensitive properties.

*terada@bk.tsukuba.ac.jp

Keywords

Permanent magnet; temperature control; inhomogeneity; single-channel shim coil

I. INTRODUCTION

Temperature is one of the essential physical or physiological parameters. Many parameters in the field of magnetic resonance imaging (MRI), such as longitudinal and transverse relaxation times (T_1 and T_2) and the diffusion coefficient, are sensitive to temperature, and MRI has the potential to map out temperature-dependent phenomena in three dimensions (3D) [1,2]. In a conventional MRI system, to measure a specimen at a specified temperature, the specimen should be stored in most cases in a temperature-regulated cell in a radiofrequency (RF) coil. However, this scheme has several drawbacks. First, the insertion of the temperature-regulated cell into the RF coil results in a decrease in the coil-filling factor, and hence in a considerable decrease in the signal-to-noise ratio [3]. Second, the temperature-regulated cell needs an optimal design to suit the RF coil that was optimized for the specimen, and this limits system versatility. Third, the specimen size is limited. A large specimen needs to be excised to fit in the small cell and be measured in vitro, which is unsuitable for measurement in vivo; otherwise only a small part of the large specimen would be thermally regulated. In this case, the temperature of most of the specimen remains unchanged, and the thermal property of the specimen cannot be measured accurately. Fourth, the heat capacity of the regulated region is small, and therefore the temperature may significantly change after specimen exchange and treatment.

These drawbacks can be overcome by *temperature regulation of the whole signal detection system including the specimen, RF coil, gradient set, and magnet*. In this scheme, no cell is needed for temperature regulation, leading to a large filling factor and high system versatility. Furthermore, stable and uniform regulation is possible even for large specimens.

For these reasons, we adopted this scheme and developed a temperature-variable MRI system with a permanent magnet placed in a cold room that could be kept at a temperature ranging from –5 °C to +10 °C [4]. We chose a permanent magnet instead of a superconducting magnet for the following reasons. A conventional MRI system with a

superconducting magnet is large and requires refilling and ventilation of the cryogen. Moreover, the cryostat vacuum seals will fail at low temperatures, in most cases. Thus temperature regulation of the overall system is unrealistic. In contrast, temperature regulation is easy in an MRI system with a permanent magnet because of compactness; moreover, permanent magnets have the advantage of bore openness and accessibility for specimens.

However, the use of a permanent magnet raises the following issues. One is the thermal drift of the magnetic field. As is well known, the remanent flux density B_r of a permanent magnet varies with temperature. Accordingly, a change in the magnet temperature during measurement leads to degradation of the spatial resolution and image artifacts, both of which are caused by the shift in the Larmor frequency. For the Nd–Fe–B permanent magnets that we used in this work, the temperature coefficient of B_r was considerably large (~1000 ppm/°C) [5], and therefore even a slight change in temperature leads to a large change in B_r and may cause serious adverse effects. However, when the temperature is regulated in the overall system, these effects are not serious because, in principle, the temperature of the magnet during measurement is the same as that of the environment.

Another, and more serious, issue is that the spatial distribution of the magnetic field also changes with temperature. In general, the permanent magnet is shimmed using many pieces of ferromagnetic material in such a way that the magnetic field is homogenous at a specific temperature [6]. However, the homogeneity deteriorates considerably with changes in magnet temperature. The resulting inhomogeneity may also cause adverse effects, such as image distortion; therefore, additional shimming may be needed according to the given system temperature.

Thus, the way the magnetic field changes spatially with temperature is an essential issue for temperature-variable MRI systems, but little information is presently available on this topic in the literature. In this paper, we first measured the variation in the magnetic field distribution of a 1.0 T yokeless permanent magnet with temperature. Then, we developed a

single-channel shim coil that was optimally designed for the measured magnetic field, and showed that high homogeneity can be achieved by shimming over a wide temperature range from –5 °C to 45 °C. Finally, we demonstrated our system using a sample from a plant.

II. MATERIALS AND METHODS

A. TEMPERATURE-VARIABLE MRI SYSTEM

Figure 1(a) shows an overview of the temperature-variable MRI system. The MRI system consisted of a small yokeless permanent magnet, a planar gradient coil set, a solenoid RF coil (Fig. 1(b)), and an MRI console. In addition, we installed a shim coil set, as follows. We first evaluated the inhomogeneity of the magnetic field without shimming (see sections IIB and IIIA). We then designed and fabricated a shim coil set and evaluated the corrected inhomogeneity (see sections IIC and IIIB). The permanent magnet, gradient coil set, RF coil, and shim coil were installed in a temperature-variable thermostatic bath with inner dimensions 620 mm (width) × 340 mm (depth) × 1154 mm (height) (FMU-263I, Fukushima Industries, Osaka, Japan). The MRI console was placed next to the thermostatic bath in the room-temperature area. The temperature of the thermostatic bath can be kept at a temperature between –15 °C and 50 °C. The control and signal lines for the gradient, RF, and shim coils were connected to the MRI console through a hole in the wall of the thermostatic bath.

The magnet (NEOMAX Engineering, Tokyo, Japan, 238 × 184 × 252 mm^3, 85 kg) had a yokeless design [7-11]. Its circuit design was the one from Ref. 10 and the same as used in Ref. 11. It was composed of Nd–Fe–B [12] permanent magnet blocks to form a Halbach magic cube in such a way that the magnetic flux was focused at the magnet gap. The magnetic field strength B_0 was 1.04 T at 25 °C and the gap was 40 mm. The homogeneity of the magnet was carefully adjusted with a passive shim technique using pieces of Nd-Fe-B magnets in a temperature-regulated room (~25 °C) in the factory (19.4 ppm over 20 mm diameter spherical volume).

We used a trapezoidal RF probe box developed for imaging of a live human finger [13]. Because the magnet gap was narrow (40 mm), we used a flat, thin gradient coil set (Fig. 1(b)). The *x*- and *y*-gradient coils were designed using the target field method modified for the planar coil [14,15], and the *z*-gradient coil was designed as a combination of circular current loops with diameters optimized using a genetic algorithm [16]. Figure 1(c) shows the wire pattern for the *x*- or *y*-, and *z*- gradient coils.

Each gradient coil element was made by winding a polyethylene-coated Cu wire (0.4 mm in diameter) and then fixed on fiber-reinforced plastic plates (90 × 90 mm^2, 0.5 mm thick) using epoxy resin. Then, the *x*, *y*, and *z* coil elements were stacked together and fixed on a rectangular plate (93 × 183 mm^2, 0.5 mm thick) using epoxy resin. The gradient coil elements were driven by a three-channel-gradient driver (±10 A, DGD10AT, Digital Signal Technology, Inc. Saitama, Japan). The efficiency of the *x*-, *y*-, and *z*-gradient coils was 27.8, 27.3, and 54.5 mT/m/A, respectively.

The RF coil was a solenoid (30 mm diameter, 35 mm long) that was shielded by a trapezoidal RF probe box made of 0.3-mm-thick brass plates (Fig. 1(b)). When the temperature was changed, the RF coil was tuned to the nuclear magnetic resonance (NMR) resonance frequency and matched to 50 Ω using three variable capacitors. The RF probe box was fixed in the gap space of the magnet.

B. EVALUATION OF THE MAGNETIC FIELD INHOMOGENEITY

The variation in magnetic field inhomogeneity was measured as follows. First, the spatial distribution of the magnetic field was measured using a 3D lattice phantom when the temperature of the magnet was at −5, 5, 15, 25, 35, and 45 °C. The phantom consisted of 11 acrylic discs (23.9 mm diameter, 3.0 mm thick) with square trenches (1.0 mm × 1.0 mm, with 3.0 mm intervals) stacked in a cylindrical container (24.0 mm inner diameter, 26.2 mm outer diameter, 62.0 mm long) filled with baby oil [4]. The 3D images of the phantom were

measured using 3D spin echo (SE) sequences (100 ms repetition time (TR), 12 ms echo time (TE), 256^3 matrix, $(125\ \mu m)^3$ voxel size) with positive and negative readout gradients. The use of readout gradients of both polarities allows the analysis to distinguish image distortions due to B_0 and gradient field inhomogeneities [17]. The spatial coordinates of the vertex points of the square lattice in the images were detected using a graphical user interface program. The inhomogeneity of the magnetic field ΔB_0 at the vertex points in the central cubic area ($(18\ mm)^3$) were calculated from positional shifts of the vertices along the readout direction. Here, ΔB_0 was defined as the difference in B_0 between the vertex point and gap center. Then, ΔB_0 was approximated using fourth-order polynomials in the Cartesian coordinates.

C. DESIGN FOR THE SINGLE-CHANNEL SHIM COIL

After the magnetic field inhomogeneity was evaluated, a shim coil set was designed to correct the inhomogeneity. To save the gap space, we used two opposite planar coils (single-channel shim coil) for shimming [18]. Details of the method are described elsewhere [19]. Briefly, the current density $\mathbf{J}(\mathbf{r})$ for the shim coil to be designed was represented as a superposition of the current density, which generates a magnetic field proportional to the second-order spherical harmonics [20], $2z^2$-x^2-y^2, x^2-z^2, y^2-z^2, or xy. Here, Cartesian coordinates x, y, and z were chosen in such a way that z and x were parallel to B_0 and the readout direction, respectively. We used only second-order terms because higher -order terms contribute little to the inhomogeneity, as will be described later. Then, the coefficient of each term was optimized using a genetic algorithm to minimize the root mean square (RMS) value of the corrected magnetic field $\Delta B_0 + B_{shim}$, where B_{shim} is the magnetic field generated by $\mathbf{J}(\mathbf{r})$. The winding pattern of the coil was derived using the stream function method [21].

D. DEMONSTRATION OF THE SYSTEM PERFORMANCE

For demonstration, a plant specimen was imaged using a 2D SE sequence (with TR 1000 ms, TE 16 and 48 ms, slice thickness 2 mm, 256^2 matrix, $(100\ \mu m)^2$ pixel) at –5 °C and 5 °C.

III. RESULTS

A. EVALUATION OF THE MAGNETIC FIELD INHOMOGENEITY

First, we evaluate the correlation between the temperature of the magnetic field and inhomogeneity without shimming. Figures 2(a) and 2(b) show the histogram of ΔB_0 and the RMS ΔB_0 in the central cubic area ($(18\ mm)^3$) for different magnet temperatures, respectively. The magnetic field was most homogenous at 25 °C (4.0 ppm RMS), where the magnet homogeneity was adjusted with the passive shim technique in the factory. As the temperature varied, the magnet field became inhomogeneous, and reached its maximum at –5 °C (16.4 ppm RMS).

Figure 3 shows the spatial distributions of the magnetic field inhomogeneity in the same cubic area, approximated using a fourth-order polynomial in the Cartesian coordinate. Although tThe first-order components largely depend on temperature and are important when one considers temperature dependence of the inhomogeneity, they were numerically subtracted, because they could be shimmed out with the gradient coils, and hence there is no need to consider them when designing the shim coil. This figure reveals that the inhomogeneity has a specific spatial symmetry, scaling linearly with temperature. The dependence of the fitting coefficients on temperature (Fig. 4) reveals which terms dominate the inhomogeneity. The cross-term coefficients were small and less important. The coefficients of the z^2, z^3, and z^4 terms at -5 °C were 1.3×10^{-2} ppm/$(pixel)^2$, -2.6×10^{-5} ppm/$(pixel)^3$, and -7.6×10^{-7} ppm/$(pixel)^4$, respectively. The corresponding inhomogeneities at the edge of the center cubic area ($18\ mm^3$) were calculated to be 46, -5.6, and -9.9 ppm,

respectively. This reveals that the second-order terms were larger than the higher-order ones and dominated the inhomogeneity variation. Furthermore, the dominant z^2, x^2, and y^2 coefficients were linearly dependent on temperature, revealing the scaling behavior of the inhomogeneity.

B. DEVELOPMENT OF SHIM COIL

The scaling behavior ensured that the magnet field inhomogeneity could be easily corrected over a wide temperature range by using a single-channel shim coil that was properly designed to compensate for the inhomogeneity at a certain temperature. According to this approach, a shim coil pattern was designed based on the result for ΔB_0 at −5 °C. Figure 5 shows the wire pattern of the shim coil.

The current flowing in the shim coil of Fig. 5 was optimized to minimize the RMS ΔB_0. Figure 6(a) shows an example of the optimization at −5 °C; the optimized current was determined to be 295 mA. As shown in Fig. 6(b), the shim current was optimized when the dominant z^2, x^2, and y^2 terms were close to zero. Unlike the z^2 term, the x^2 and y^2 terms were not negligible but they were equal in magnitude and opposite in sign, leading to the reduction in the total inhomogeneity. Thus, the shimming was appropriately designed to compensate for the dominant terms. Figure 6(c) shows 2D slices selected from 3D image datasets acquired with and without shimming. The images without shimming exhibit the distortion in the readout direction, which originated from the inhomogeneity and was drastically corrected by shimming.

The shim current was similarly optimized for different temperatures as follows. First, at each temperature, the RMS ΔB_0 vs shim current was plotted. Then, the optimized current where the RMS ΔB_0 was at a minimum was determined. Figure 7(a) shows the optimized current as a function of temperature. The optimized current has a linear dependence on temperature, which is in good agreement with the scaling behavior of ΔB_0. Figure 7(b) shows

the histograms of ΔB_0 measured at the shim currents optimized at each temperature. This shows that the variations in ΔB_0 were much smaller than those without shimming (Fig. 2(a)). With shimming, the RMS values (Fig. 7(c)) and second-order coefficients (Fig. 7(d)) became also fairly smaller, independent of temperature. These results were highly reproducible. As will be discussed later, these results provide evidence that the shimming works well even when the temperature varies.

C. DEMONSTRATION

As an application of the temperature-variable MRI system, we acquired 2D images of a small vegetable, okra pod (~18 mm in diameter and ~10 cm in length) at different temperatures. First, we confirmed the shimming effect on imaging. An MR image acquired without shimming (Fig. 8(a)) showed the large distortion, which was corrected by shimming (Fig. 8(b)), as was distinguished in the difference image (Fig. 8(c)).

Figures 9(a) and 9(b) show MR images acquired at 5 °C for different TE values. Tissues with high water content are brightly imaged in Fig. 9(a), and it is possible to distinguish the organization of tissue structures, such as the pericarp, cavities, and seeds, and intrastructures of the pericarp, such as vascular bundles. Meanwhile, the image acquired with longer TE (Fig. 9(b)) exhibits a different contrast, especially at the vascular bundles in the pericarp. The contrast difference is associated with the difference in the T_2 value, and the brighter area in Fig. 9(b) corresponds to the tissues with the longer T_2. This was ascertained by the T_2 image (Fig. 9(c)), which was calculated numerically from the images shown in Figs. 9(a) and 9(b). It is likely that the free water was responsible for the long T_2 value. In contrast, for –5 °C (Figs. 9(d) and 9(e)), the signal intensity at the vascular bundles decreased strongly, and the image contrast in the pericarp was almost the same. Furthermore, T_2 was almost

constant and short in the pericarp (Fig. 9(f)). These indicate that the free water in the vascular bundles was almost frozen at –5 °C.

IV. DISCUSSION

The spatial distribution of the magnetic field has a specific feature. The second-order coefficients z^2, x^2, and y^2 dominated the inhomogeneity variation and were linearly scaled with temperature. One possible factor affecting the observed thermal behavior is the geometric distortion of the magnet circuit due to thermal expansion and contraction. The homogeneity of the magnetic field is mainly determined by arrangement and configuration of pole pieces (made of iron and silicon steel plates) with small protrusion (Rose shim [22]). Since the thermal expansion coefficients are different between Nd-Fe-B magnets ($\sim 10^{-6}$) and pole pieces ($\sim 10^{-5}$), the temperature change would cause an error in relative positioning of the pole pieces and main magnets. As the temperature rises, the radius of the pole pieces may become relatively larger, which may result in the decrease in the z^2 coefficient and the increase in the x^2 and y^2 coefficients. This qualitatively agrees with the result in Fig. 4.

Another factor is the thermal variation in the magnetic properties. As the temperature varies, B_r for the Nd-Fe-B magnet changes linearly at a rate of –0.1 %/°C. Therefore, the spatial distribution of the magnetic field may also vary linearly with temperature. However, the observed change in the second-order coefficients were much larger (–19 %/°C for the z^2 coefficient) and the changes in sign cannot be explained, indicating that this interpretation is oversimplified.

As discussed above, the understanding of the observed temperature dependence is not straightforward, though the observed scaling behavior is quite simple. This is mainly because the magnetic circuit has a complicated structure composed of many materials, and each component has different geometrical and magnetic responses to temperature. Moreover, many imperfections (positioning, magnetization heterogeneities from fabrication,

demagnetization, etc.) contributing to the inhomogeneity also depend on temperature, which complicates the issues. The detailed study using 3D simulation including the thermal coefficients of magnetic properties as well as the structure constants will give a quantitative explanation for the inhomogeneity variation.

The scaling behavior enabled us to compensate for the inhomogeneity over a wide temperature range with the single-channel shim coil. With shimming by the specially designed coil, the RMS ΔB_0 decreased drastically from 16.4 to 5.7 ppm at –5 °C, which was close to the minimum value (4.0 ppm) at 25 °C. The key results are that the residual second-order terms were largely temperature independent (Fig. 7(d)) and that they were much smaller than those without shimming (Fig. 4). These indicate that the second-order adjustments are effective and have been optimized.

In the previous paper [4], because the dependence of the inhomogeneity on temperature was unknown, the inhomogeneity was compensated for with a number of high-order coils (xy, x^2-y^2, z^2, and z^3) according to the conventional Anderson approach [23]. In contrast, in the present system, we adopted the single-channel coil design. This offers the advantages of simplicity of shimming and a larger available volume of the gap space.

The temperature drift during imaging was slight but not negligible because the temperature regulator was switched off to avoid the external electromagnetic noise coming into the imaging area. For example, the Larmor frequency shifted from 45.8061 to 45.7600 MHz during the ~2 h 3D SE measurement at –5.5 °C, which corresponded to an increase of 1.1 °C in the magnet temperature. The temperature drift may cause adverse effects on imaging such as degradation of the spatial resolution. However, this can be largely overcome by an NMR lock technique [24], as was shown in the high-resolution MR images obtained with this technique (Figs. 8 and 9). Moreover, the additional field inhomogeneity may appear because of the heat produced by the gradient coils, especially when the temperature regulator is switched off. However, this was unlikely to occur, because the heat was

estimated to be quite small (~1W) and the heat capacity of the magnet was quite large. More accurate regulation of temperature would be possible if a more sophisticated shield technique, which enables temperature regulation during measurement, was introduced, and/or if a noiseless subsidiary temperature regulator was added.

In addition to the temperature drift, varying the temperature of the entire magnet has a disadvantage of a long equilibration time (typically several hours) after a temperature change. Thus, a rapid thermal response of a specimen cannot be measured at present. However, introduction of a powerful air circulation system would reduce the equilibration time.

V. CONCLUSION

We have developed a temperature-variable MRI system using a yokeless 1.0 T permanent magnet. We first evaluated the inhomogeneity of the magnetic field at temperatures from –5 °C to 45 °C. The series expansion analysis revealed that the inhomogeneity had the specific spatial characteristics; the second-order terms z^2, x^2, and y^2 were dominant in this order and they scaled linearly with temperature. This scaling behavior revealed that the spatial inhomogeneity of the magnetic field was mainly determined by the geometric layout of the magnetic circuit, and that it changed only in magnitude as the temperature varied. The simple scaling law ensures that the magnet field inhomogeneity can be corrected over a wide temperature range by using a single-channel shim coil that is properly designed to compensate for the inhomogeneity at a certain temperature. Accordingly we designed and fabricated the single-channel shim coil. With shimming, the RMS ΔB_0 decreased drastically over the wide temperature range. As an application of the temperature-variable MRI system, we acquired 2D images of an okra pod at –5 °C and +5 °C. These images exhibited a clear contrast, reflecting the freezing behavior of free water.

ACKNOWLEDGMENTS

We thank Dr. T. Haishi for technical assistance.

Reference

[1] S. Stapf, Song-I Han ed. NMR Imaging in Chemical Engineering, Wiley-VCH, Weinheim, 2006.

[2] S. L. Codd, J. D. Seymour ed. Magnetic Resonance Microscopy, Wiley-VCH, Weinheim, 2009.

[3] D. I. Hoult, R. Richards, Signal-to-noise ratio of nuclear magnetic-resonance experiment, J. Magn. Reson. 24 (1976) 71-85.

[4] S. Adachi, T. Ozeki, R. Shigeki, S. Handa, K. Kose, T. Haishi, M Aoki, Development of a compact magnetic resonance imaging system for a cold room, Rev. Sci. Instrum. 80 (2009) 054701.

[5] NEOMAX magnet catalog:
http://www.hitachi-metals.co.jp/prod/prod03/pdf/hg-a22-b.pdf

[6] M. Aoki, US Patent No. 6,448,772 (2002).

[7] K. Halbach, Design of permanent multipole magnets with oriented rare earth cobalt material, Nucl. Instrum. Methods. 169 (1980) 1-10.

[8] H. Zijlstra, Philips, Permanent-magnet systems for NMR tomography, J. Res. 40 (1985) 259-288.

[9] H. A. Leupold, E. Potenziani II, M. G. Abele, Applications of yokeless flux confinement, J. Appl. Phys. 64 (1988) 5994-5996.

[10] M. Aoki and T. Tsuzaki, US Patent No. 7,084,633 (2006).

[11] T. Shirai, T. Haishi, S. Utsuzawa, Y. Matsuda, K. Kose, Development of a compact mouse MRI using a yokeless permanent magnet, Magnetic Resonance in Medical Sciences, 4 (2005) 137-143.

[12] M. Sagawa, S. Fujimura, N. Togawa, H. Yamamoto, Y. Matsuura, New material for permanent-magnets on a base of Nd and Fe, J. Appl. Phys. 55 (1984) 2083-2087.

[13] N. Iita, S. Handa, S. Tomiha, and K. Kose, Development of a compact MRI system for measuring the trabecular bone microstructure of the finger, Magn. Reson. Med. 57 (2007) 272-277.

[14] R. Turner, A target field approach to optimal coil design, J. Phys. D: Appl. Phys. 19 (1986) L147-L151.

[15] J. Jianming, Electromagnetic Analysis and Design in Magnetic Resonance Imaging, CRC, Boca Raton, FL, 1998.

[16] D. E. Goldberg, Genetic Algorithms in Search, Optimization and Machine Learning, Addison-Wesley Longman Publishing, Boston, 1989.

[17] A. Kawanaka, M. Takagi, Estimation of static magnetic field and gradient fields from NMR image, J. Phys. E: Sci. Instrum.19 (1986) 871-875.

[18] R. Shigeki, K. Kose. A single-channel planar shim coil for a permanent magnet, Proc. Intl. Soc. Mag. Reson. Med. 18 (2010) 1542.

[19] D. Tamada, Y. Terada, K. Kose. Bi-planar shim coil designed by stream function method improves B0 homogeneity along z-axis, Proc. Intl. Soc. Mag. Reson. Med. 19 (2011) 3793.

[20] F. Roméo, D. I. Hoult, Magnet field profiling: analysis and correcting coil design, Magn. Reson. Med. 1 (1984) 44-65.

[21] M. A. Martens, L. S. Petropoulos, R. W. Brown, J. H. Andrews, Insertable biplanar gradient coils for magnetic-resonance-imaging, Rev. Sci. Instrum. 62 (1991) 2639-2645.

[22] M. E. Rose, Magnetic field corrections in the cyclotron, Phys. Rev. 53 (1938) 715-719.

[23] W. A. Anderson, Electrical current shims for correcting magnetic fields, Rev. Sci. Instrum. 32 (1960) 241-250.

[24] T. Haishi, T. Uematsu, Y. Matsuda, K. Kose, Development of a 1.0 T MR microscope using a Nd-Fe-B permanent magnet, Magn. Reson. Imaging 19 (2001) 875-880.

Figure captions

Fig. 1 (a) Overview of the temperature-variable MRI system. (b) Schematic of the RF probe box that is inserted into the magnet gap. (c) Wire patterns for the coils for the *z*-gradient (G_z) and for the *x*- and *y*-gradients (G_x and G_y).

Fig. 2 Evaluation of magnetic field inhomogeneity ΔB_0 without shimming. (a) Histograms of ΔB_0 for different temperatures. (b) RMS ΔB_0 as a function of temperature. The solid line is a visual guide.

Fig. 3 Spatial distribution of ΔB_0 for different temperatures estimated in the central cubic area ($(18\ \mathrm{mm})^3$). Lower and upper thresholds for volume rendering are –2.5 (blue) and +2.5 ppm (red), respectively.

Fig. 4 Temperature dependence of the fitting coefficients of ΔB_0 (some negligibly small coefficients were omitted); the solid lines is show the linear fit to data.

Fig. 5 Wire patterns of the specially designed single-channel shim coil set.

Fig. 6 Example of the optimization of shim current at –5 °C. (a) RMS ΔB_0 as a function of shim current. The solid line is a visual guide. (b) Fitting coefficients as a function of shim current; linear fits to the x^2, y^2, and z^2 components are shown as solid lines. (c) 2D slices selected from 3D SE image datasets acquired (upper) with optimal shimming and (lower) without shimming. The lengths indicated on top are distances from the center in the *y*-axis direction.

Fig. 7 Evaluation of shimming. (a) Current optimized to minimize ΔB_0 for different temperatures. The solid line shows the linear fit to data. (b) Histograms, (c) RMS, and (d) fitting coefficients of ΔB_0 measured at the optimized currents. In (b), RMS ΔB_0 without shimming shown in Fig. 2(b) are plotted for comparison.

Fig. 8 MR images of an okra pod obtained (a) with and (b) without optimized shimming. The difference image between (a) and (b) is shown in (c).

Fig. 9 MR images of an okra pod (a) obtained at TE = 16 ms, 5 °C, (b) obtained at TE = 48 ms, 5 °C, (c) T_2 image for 5 °C calculated from (a) and (b); (d) obtained at TE = 16 ms, –5 °C, (e) TE = 48 ms, –5 °C, (f) T_2 image for 5 °C calculated from (d) and (e). TR = 1000 ms and slice thickness = 2 mm for all images.

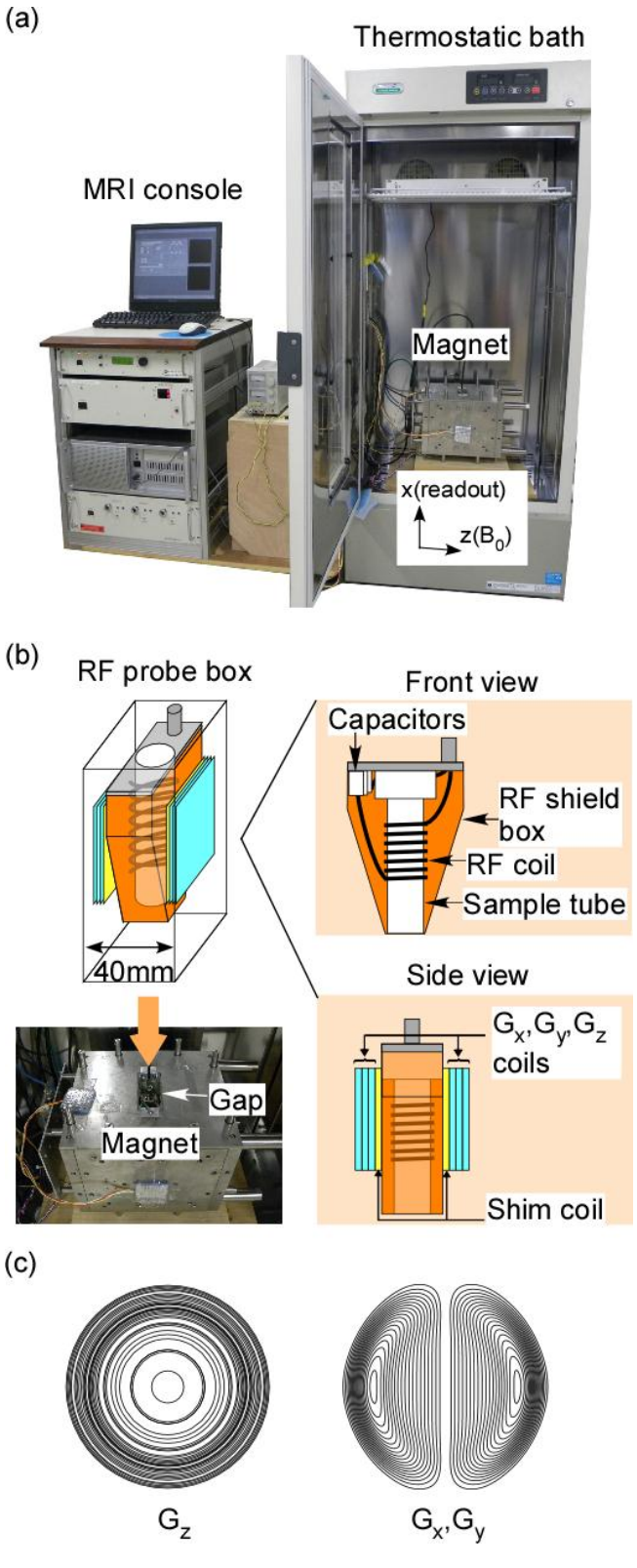
(a)
Thermostatic bath
MRI console
Magnet
x(readout)
z(B0)
(b)
RF probe box
Front view
Capacitors
RF shield box
RF coil
Sample tube
40mm
Side view
Gx,Gy,Gz coils
Gap
Magnet
Shim coil
(c)
Gz
Gx,Gy

Fig. 1

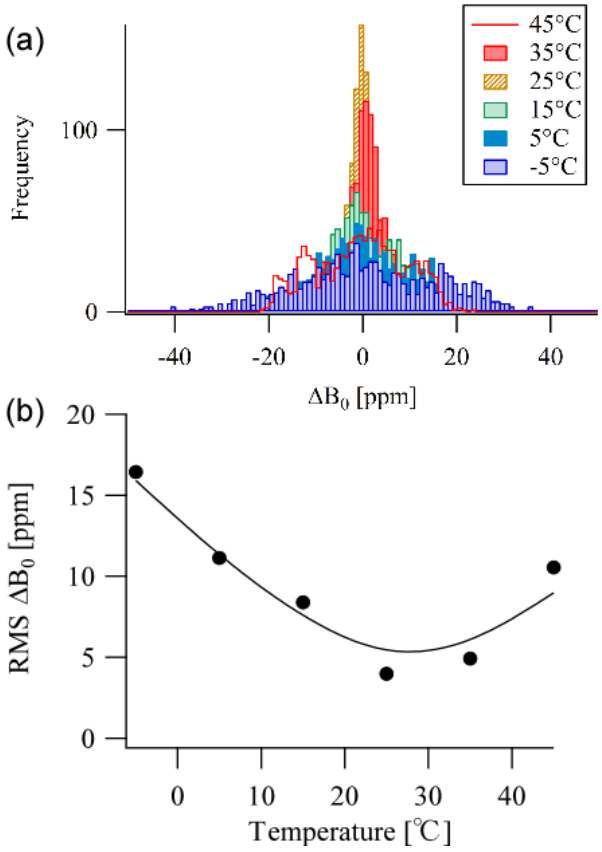
(a)
45°C
35°C
25°C
15°C
5°C
-5°C
Frequency
100
0
-40
-20
0
20
40
ΔB0 [ppm]
(b)
20
15
10
5
0
RMS ΔB0 [ppm]
0
10
20
30
40
Temperature [℃]

Fig. 2

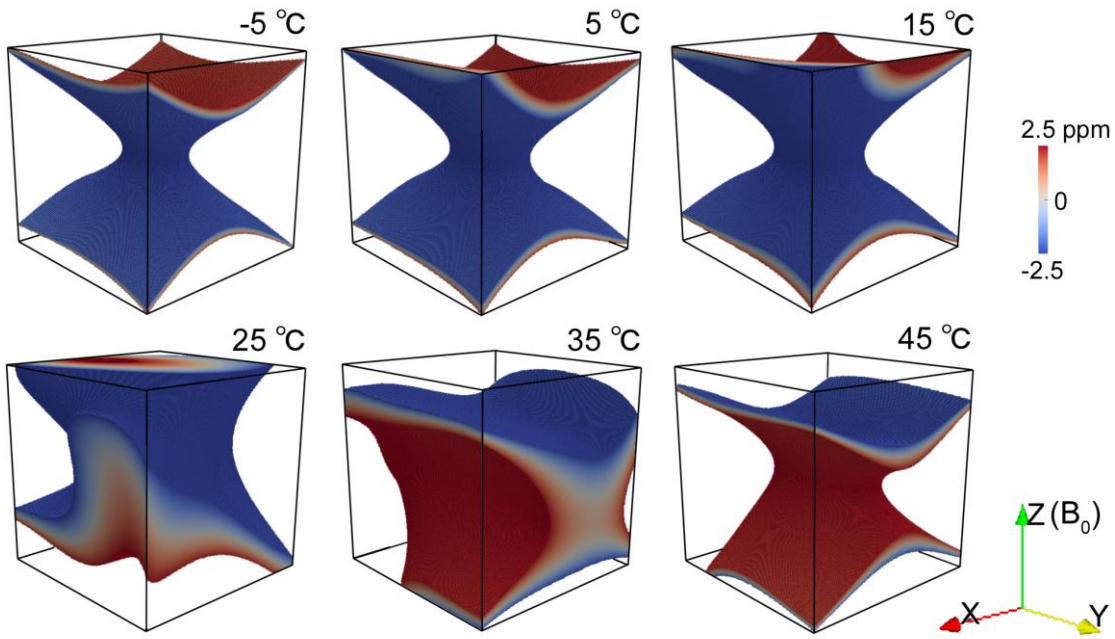

Fig. 3

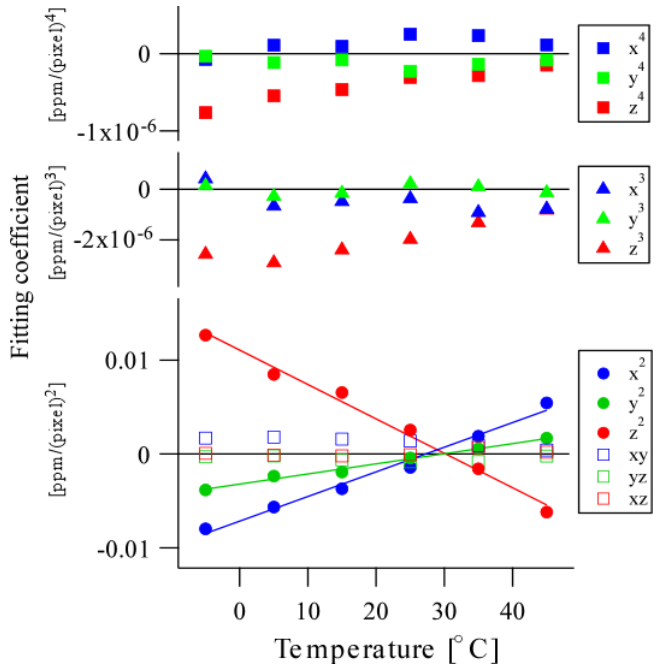
Fitting coefficient
[ppm/(pixel)^4]
0
-1x10^-6
x^4
y^4
z^4
[ppm/(pixel)^3]
0
-2x10^-6
x^3
y^3
z^3
[ppm/(pixel)^2]
0.01
0
-0.01
x^2
y^2
z^2
xy
yz
xz
0
10
20
30
40
Temperature [°C]

Fig. 4

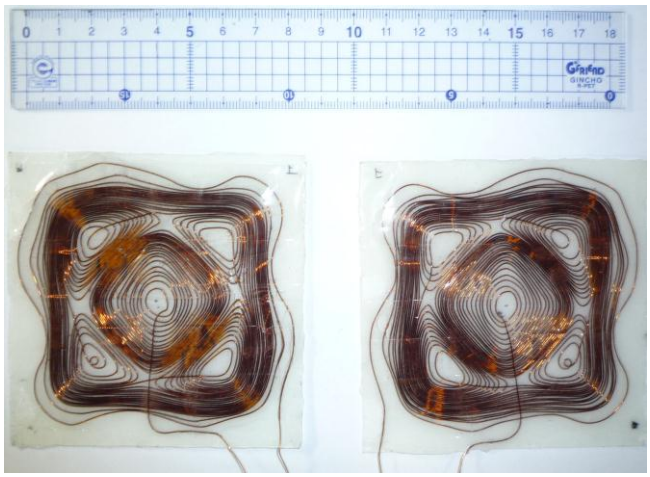

Fig. 5

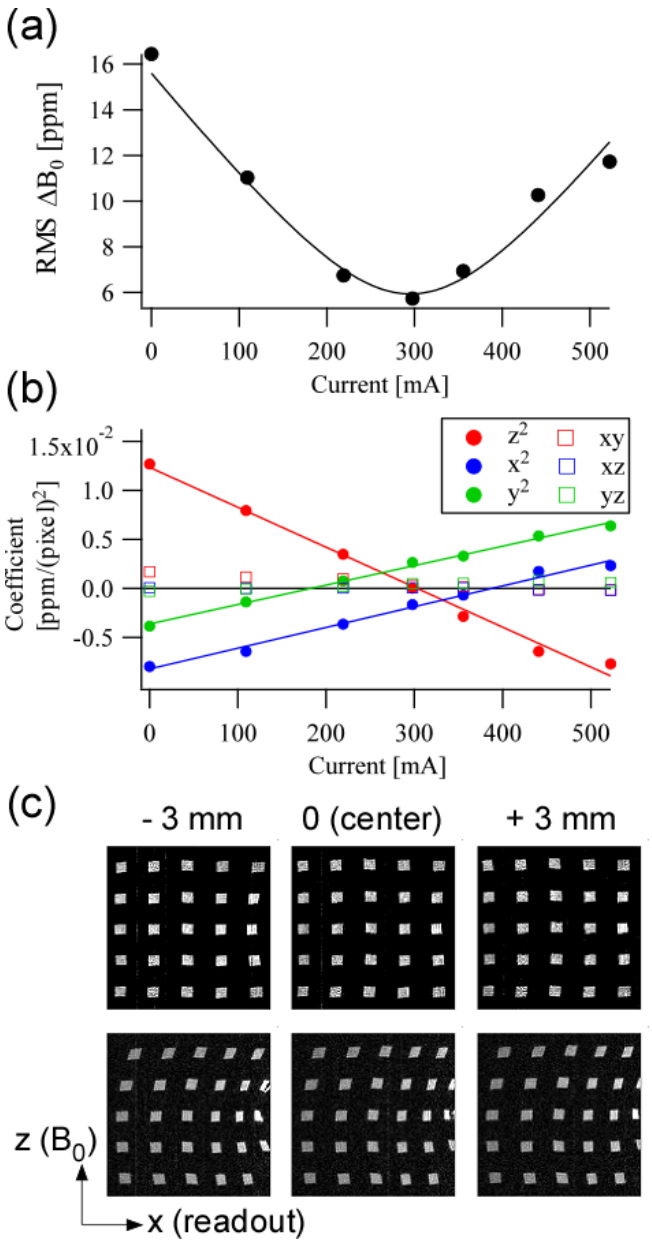
(a)
RMS ΔB0 [ppm]
16
14
12
10
8
6
0
100
200
300
400
500
Current [mA]
(b)
Coefficient [ppm/(pixel)2]
1.5x10-2
1.0
0.5
0.0
-0.5
z2
x2
y2
xy
xz
yz
0
100
200
300
400
500
Current [mA]
(c)
- 3 mm
0 (center)
+ 3 mm
z (B0)
x (readout)

Fig. 6

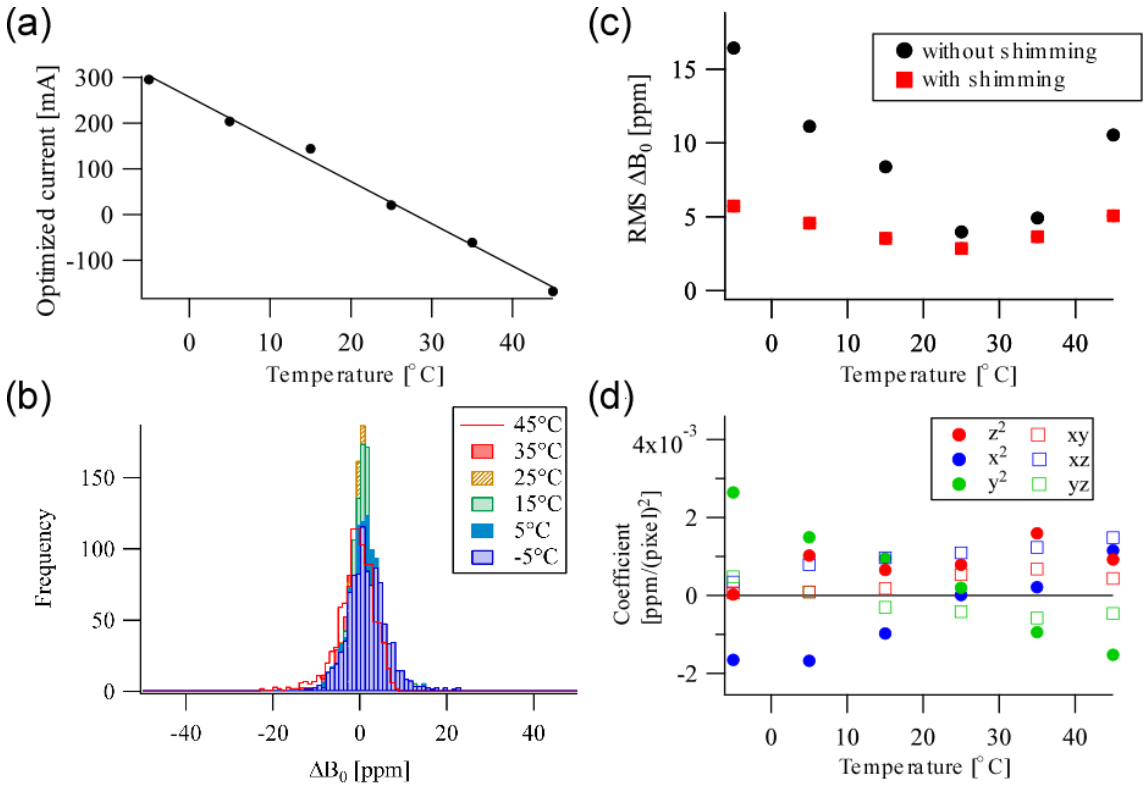
(a)
Optimized current [mA]
300
200
100
0
-100
0
10
20
30
40
Temperature [°C]
(b)
Frequency
150
100
50
0
-40
-20
0
20
40
ΔB0 [ppm]
45°C
35°C
25°C
15°C
5°C
-5°C
(c)
RMS ΔB0 [ppm]
15
10
5
0
without shimming
with shimming
Temperature [°C]
(d)
Coefficient [ppm/(pixel)2]
4x10-3
2
0
-2
z2
x2
y2
xy
xz
yz
Temperature [°C]

Fig. 7

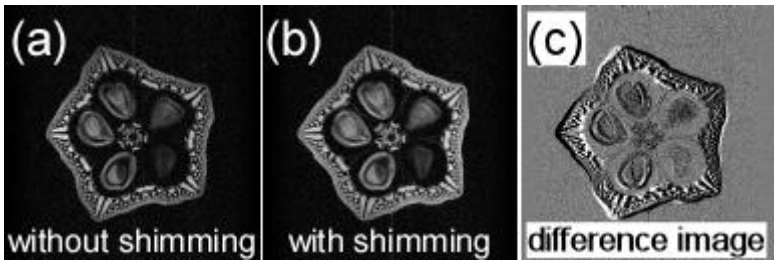

Fig. 8

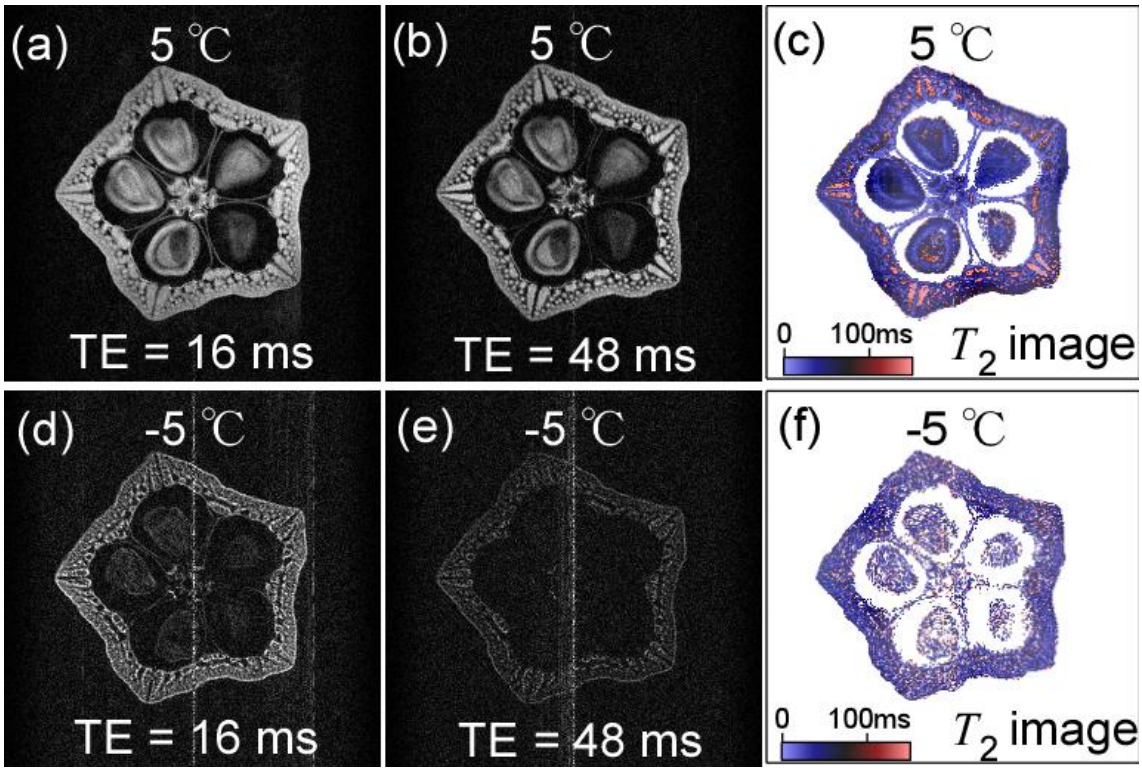
(a) 5 ℃
TE = 16 ms
(b) 5 ℃
TE = 48 ms
(c) 5 ℃
0 100ms
T_2 image
(d) -5 ℃
TE = 16 ms
(e) -5 ℃
TE = 48 ms
(f) -5 ℃
0 100ms
T_2 image

Fig. 9